Chapter 5

Imaging the Tumor Response to the Tumor-penetrating Peptide iRGD

Improvement of drug uptake into the tumor mass is highly desirable. Recently, a tumor-penetrating peptide, iRGD, has been shown to improve the uptake of a number of different classes of drugs into the tumor mass without seeming to alter the pharmacokinetics of the drugs in other tissues. Translation of iRGD to the clinic would be facilitated by a noninvasive assay that can identify patients sensitive to iRGD. Furthermore, a noninvasive assay may provide further insights into the *in vivo* mechanism of iRGD. We hypothesize that iRGD can modulate the uptake of MRI and PET-visible contrast agents by altering the perfusion characteristics of the tumor. We hypothesize that this modulation would be visible by DCE-MRI, diffusion MRI and PET.

In this chapter, we present preliminary results of MRI and PET experiments probing the tumor response to iRGD. The results show that DCE-MRI may be a potentially useful tool to visualize iRGD response in the clinic. However, further investigations into the effects of iRGD in animal models of cancer needs to be pursued to build on these results.

Acknowledgments: We thank Drs. Kazuki Sugahara, Tambet Tessalu and Erkki Ruoslahti for interesting discussions and for providing the mice for these studies, Dr. Andrey Demyanenko, Dr. Sharon Lin, Dr. Xiaowei Zhang, Dr. Kofi Poku, Naomi Santa Maria, Desiree Crow, and Junie Chea for their technical assistance. Drs. Andrew Raubitschek, David Colcher provided the Herceptin and provided welcome feedback. Drs. Shengxiu Li, David Koos and Scott Fraser provided useful advice. The project is funded by a NCI STRAP grant (P01 CA043904), City of Hope Lymphoma SPORE Grant (P50 CA107399), the Beckman Institute and the Caltech/City of Hope Biomedical Initiative.

5.1 Introduction

5.1.1 CendR Rule

Teesalu *et al.* identified a peptide motif (via phage display) which mediated uptake of labelled phage into a variety of tumor cells [50]. The motif consists of RXXR. They found that this motif needs to be at the C-terminus of the peptide chain (either endogenously or exposed by enzymatic cleavage) to be active (thus the CendR rule). Furthermore, they discovered that the motif interacts with the neuropilin-1 receptor, a mediator in the VEGF pathway [243, 244]. VEGF165A, a potent mediator of vascular permability, contains the CendR motif. Incorporation of multimeric CendR peptides increased vascular permeability and uptake of CendR-labelled phage into lung and subcutaneous tissue. Interestingly, several viruses express the CendR sequence on their membrane and envelope proteins.

5.1.2 iRGD

CendR peptides have no specific tissue homing ability. Sugahara *et al.* identified a class of CendR peptides that contain the RGD motif [48]. The RGD motif has been well characterized to bind to α_v integrins receptors, which are often overexpressed in tumor blood vessels and have been used to target agents to tumor blood vessels [245, 136]. CendR-containing, internalizing-RGD (iRGD) peptides, when linked to nanoparticles, phage and micelles increased their tumor penetration significantly. In a BT474 xenograft mouse model, iRGD-Abraxane concentration in tumors were increased 10-fold over Abraxane alone.

In a subsequent study, Sugahara *et al.* further demonstrated that iRGD effects can be mediated without linkage of the peptide to the agent of interest [49]. Coadministration of iRGD was shown to increase tumor penetration of a small-molecule doxorubicin, doxoruibin-containing liposomes, and the antibody trastuzumab. iRGD's *in vivo* mechanism of action remains unclear. It is postulated that the RGD motif allows tumor homing. An as yet unknown protease is responsible for the peptide cleavage, exposing the CendR motif. Interaction of the CendR motif with the neuropilin-1 receptor results in both increased vascular permeability and increased tumor cell uptake of agents. The contribution of both mechanisms to effective drug uptake remains unknown. Indeed, the ac-

tion of neuropilin-1 expression in tumors is complex and remains unclear [246, 247]. The exact timing of uptake efficacy is also unknown, although significant uptake increases of coadministered agents have been shown within a 30 minute to 3 hour time window post iRGD injection (private communication, K.S.).

5.1.3 Noninvasive Measures of Vascular Permeability with MRI

DCE-MRI is a commonly used method to evaluate vascular permeability in tumors (see section 2.3.2.2). The majority of DCE-MRI studies focus on either differentiating tumor grades or studying the vascular modulation as a result of antiangiogenic therapies. Angiogenic factors within tumors are often dysregulated, favoring neovascularization rather than vessel maturation [248, 249]. As a result, tumor blood vessels are often tortuous and leaky. The basis behind this is incompletely understood. However, many studies have shown that increased tumor leakiness, measured by DCE-MRI, correlates with tumor grade and malignant potential [250, 251, 252]. Permeability has also been correlated with other tumor microenvironmental factors, such as hypoxia [253].

Folkman hypothesized that cutting off the tumor blood supply is a viable anti-tumor strategy [254]. This has led to the development of several antiangiogenic and vascular disruptive therapies for cancer. DCE-MRI has shown potential to monitor the effects of these therapies [255, 221]. Decreases in permeability parameters (e.g.K_{trans}) has been demonstrated as a positive biomarker of antiangiogenic treatment efficacy [256, 131, 257].

For both tumor phenotyping and treatment response scenarios, tumor vascular changes usually occur over days to months. We hypothesize that iRGD increases the uptake of MRI-visible contrast agents via an increase in vascular permeability and that this occurs within a short timescale (<30 minutes). Few studies have explored the use of DCE-MRI to measure drug-modulated increases in vascular permeability, expecially at such a short timescale. Su *et al.* observed pharmacokinetic changes of Gd-DTPA uptake immediately after the intravenous application of angiotensin II, hydralazine and histamine [258]. Tumor enhancement was decreased in the presence of all three modulators. Only the vasodilator histamine delayed Gd-DTPA washout. Wang *et al.* investigated the hydralazine response using Gd-DTPA-Albumin, observing a decrease in the tumor blood volume fraction occupied by the contrast agent [259].

The effect of localized angiogenic stimuli has also been monitored by DCE-MRI. Dafni *et al.* observed increased dermal permeability to Gd-DTPA-Albumin in response to intradermal injection of VEGF165 within 30 minutes of administration [260]. In a separate study, they also showed that VEGF165 attenuation in tumors decrease Gd-DTPA-Albumin within 48 hours in a C6 cell line with tetracycline-inducible VEGF expression [261]. Recently, Cartwright *et al.* also showed increased permeability and vascular changes of urinary bladder tissue in the presence of a VEGF121-containing graft-matrix over a 3-week period using Gd-DTPA [262]. These results suggest that tumor permeability increases mediated by iRGD may be probed by DCE-MRI.

5.2 Materials and Methods

5.2.1 Preparation of compounds

iRGD's structure is described elsewhere [48]. iRGD was synthesized commercially (Bachem) and lyophilized for long term storage. Aliquots of iRGD for individual studies were made up in 1 × PBS and stored at –80°C until use. Tests on this material demonstated that iRGD was stable at 4°C for at least 2 weeks (private communication, A.R.).

Platelet-activating factor (PAF, Sigma-Aldrich, P4904) was diluted with 1 × PBS, aliquoted and stored at –20°C until use.

5.2.2 Cells and Tumor Models

The HER2-expressing BT474 human breast cancer cell line was cultured in SFM4MAB medium with 10% fetal bovine serum and penicillin/streptomycin. 17β-estradiol pellets (Innovative Research of America) were implanted subcutaneously into the back of the athymic BALB/c nude mice one day prior to orthotopic innoculation (6th and 9th mammary fat pad) of 5×10^6cells in matrigel (BD Biosciences). Tumors were ~2–300 mm^{3}at the time of imaging. Mouse care and experimental procedures were carried out in accordance with protocols approved by the Research Animal Care Committees at the Sanford Burham Institute, City of Hope and Caltech.

5.2.3 MRI-only Studies

A timeline for MRI-only studies is shown in figure 5.1. Before each imaging session, each mouse is catheterized with a 30G needle attached to PE10 tubing in the tail vein for contrast agent and peptide administration inside the MRI. Baseline and treatment imaging sessions were separated by ~3 hours to allow adequate washout of CA from the first scan (Gd-DTPA, Magnevist, Bayer, plasma half-life = 12 minutes in mice).

5.2.3.1 Anatomical MRI

A Biospec (Bruker-Biospin Inc., Billerica, MA) 7 T MRI scanner and a home-built birdcage coil with an 8 cm axial field of view (FOV) were used for mouse MRI image acquisition. For all imaging sessions, animals were anesthetized using a 1.3%–1.5% isoflurane/air mixture and body temperature was maintained at 36°C–37°C with warmed air flowing through the bore. For anatomical imaging, a RARE sequence (TR/TE = 4000/23 ms; RARE factor = 4; number of averages = 2; FOV = 35.4 × 35.4 mm^2; image matrix = 128 × 128; slice thickness = 0.754 mm) was used to collect 40 contiguous images across the mouse torso, allowing tumor visualization.

5.2.3.2 T_1 mapping

A variable flip angle method outlined in section 3.1.1.3 was used to generate T_1 maps. Gradient echo images (FLASH, FA = 12°, 24°, 36°, 48°, 60°, matrix size = 140 × 80, voxel size = 0.25 × 0.25 mm^2, slice thickness = 1 mm, TR/TE = 200/2 ms) centered on the tumor (3 slices) and the left ventricle (1 slice) were acquired.

5.2.3.3 DCE-MRI

After T_1 maps were acquired, 0.9% saline, 10 nmol/kg PAF or 0.2 mg/mouse iRGD in a volume of 0.1 mL was injected into the mouse, followed by a 0.1 mL saline chase to clear the catheter. 12 minutes was allowed to elapse prior to starting the DCE-MRI scan. The DCE-MRI time series were acquired using a gradient echo sequence (FLASH, FA = 35°, TR/TE = 25/2 ms, geometry the same as the T_1 maps, time resolution = 2 s, duration = 22 minutes). After a baseline of 2.5 minutes, Gd-DTPA (0.1 mmol/kg per DCE-MRI scan) was injected intravenously via the catheter using a

powered-injector (New Era Inc., Farmingdale N.Y.) at 0.5 mL/min.

To retain good spatial coregistration between baseline and treatment scans, mice were secured in the animal holder between the two imaging sessions obtained on the same day. The holder was placed on a warm electric blanket outside the MRI to keep the mice warm during this period (~3.5 hours, to allow for CA washout). A motorized stage enabled exact repositioning of the holder in the MRI. Mice were kept lightly anesthesized using ~0.5%–0.7% isofluorane. Lactate Ringer's solution (0.15 mL per mouse) was injected subcutaneously halfway through the intersession period to reduce metabolic acidosis. Mice were kept in their home cage at all other times. All the MRI scans described above were performed for both baseline and treatment scan sessions. A total of 10 mice were used in this study. Half (N = 5) were treated on the first day with PAF, while the other half (N = 5) were treated with iRGD on the first day. Treatments were reversed on day 3.

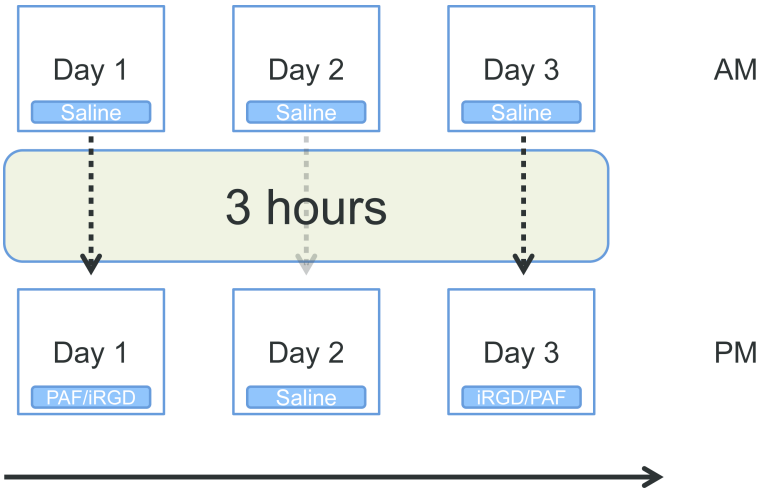

Figure 5.1: Study design for iRGD MRI. Each BT474-bearing mouse was imaged on three consecutive days. Each day consisted of two DCE-MRI scan sessions. PAF or iRGD was injected intravenously 15 minutes before the second DCE-MRI scan on day 1. The alternative treatment was administered on day 3. Saline was administered on day 2. 3 hours were allow to elapse between baseline and treatment scans to allow adequate CA washout.

5.2.3.4 Image Analysis

DCE-MRI data were analyzed with the extended Kety model [82]. The model incorporates the exchange of CA between the extracellular vascular space (plasma) and the tissue extracellular space (figure 2.3). The influx rate of CA moving from the plasma to tissue space is denoted K_{trans}. The efflux rate from the tissue back to the plasma is related to the extracellular volume fraction v_e by

$\frac{K_{trans}}{v_e}$. Assuming instantaneous homogeneous distribution of CA in both compartments, the model can be described by

$$\frac{d}{dt}C_t(t) = K_{trans}C_p(t) - (\frac{K_{trans}}{v_e})C_t(t). \tag{5.1}$$

$C_t(t)$ and $C_p(t)$ are the concentrations of CA in tissue and plasma respectively. The solution to this equation is

$$C_t(t) = K_{trans}\int_0^t C_p(u)e^{-(\frac{K_{trans}}{v_e})(t-u)}du. \tag{5.2}$$

This equation neglects the vascular volume in the tissue, which may be invalid in pathological tissues. The model can be extended to include a vascular fraction component v_p:

$$C_t(t) = K_{trans}\int_0^t C_p(u)e^{-(\frac{K_{trans}}{v_e})(t-u)}du + v_pC_p(t). \tag{5.3}$$

$C_t(t)$ and $C_p(t)$ are obtained from the dynamic time series. ROIs drawn over the tumor and left ventricle (LV) were used for $C_t(t)$ and $C_p(t)$ respectively. Signal intensity for each voxel in the ROIs was first converted to $R_1 = 1/T_1$:

$$R_1(t) = \frac{1}{TR}ln\left(\frac{(S_0 sin\alpha e^{-TE/T_2^*}) - S(t)cos\alpha}{(S_0 sin\alpha e^{-TE/T_2^*}) - S(t)}\right). \tag{5.4}$$

R_1, TR, TE described previously, α is the flip angle, $T_2^* >> TE$, $S(t)$ is the signal intensity time course and:

$$S_0 = S_{SS}\frac{(1-e^{-TR/T_1}cos\alpha)}{(1-e^{-TR/T_1})sin\alpha e^{-TE/T_2^*}}. \tag{5.5}$$

S_{SS} is the steady state average signal intensity before CA administration. $R_1(t)$ is converted to $C(t)$ using the fast exchange limit assumption:

$$R_1 = r_1(1-h)C + R_{10}. \tag{5.6}$$

$r_1$is the relaxivity of Gd-DTPA at 7 T (4.71 s^{-1} mM^{-1}), h is the hematocrit of a mouse (h = 0.45 based on literature values) and R_{10} is derived from the T_1 map.

Calculation of $C_p(t)$, the arterial input function (AIF) is a subject of intense investigation. For this study, we adopted an image-based method similar to Loveless *et al.* [263]. For our studies, voxels with SNR <5 at all time points in the LV ROI on each individual dataset were first removed. Next, each voxel in the ROI was visualized individually. Voxels that do not show a time curve reflecting plasma uptake (i.e.fast uptake, rapid washout) were further excluded. The remaining voxels were averaged together to represent the individual AIF for the particular study (AIF_{ind}). Each AIF_{ind} was fitted to a model derived by MacGrath *et al.* [264], described as a mixture of a Gaussian and an exponential modulated by a sigmoid:

$$C_p(t) = \begin{cases} 0 & , \quad t \leq t_0, \\ \sum_{n=1}^{N} \frac{A_n}{\sigma_n\sqrt{2\pi}} e^{\left(\frac{-(t-T_n-t_0)^2}{2\sigma_n^2}\right)} + \frac{\alpha e^{-\beta(t-t_0)}}{(1+e^{(-s(t-\tau-t_0))})}, & t \geq t_0, \end{cases} \tag{5.7}$$

where N = 1, A_n, T_n and σ_n are the scaling constants, centers and widths of the *nth* Gaussian; α and β are the amplitude and decay constant of the exponential; s and τ are the width and center of the sigmoid respectively. t_0 marks the start time of CA injection. The Gaussian constants are related to the speed of injection and the shape and concentration of the bolus, while the other constants are related to the decay of the CA in the plasma. We chose this model as opposed to other models described in the literature because it gave the best visual fit among all the AIFs considered in this study. Most AIFs showed a maximum peak concentration of approximately 2.5–3 mM, peaking at approximately 15 seconds post CA injection. The AIFs measured for one mouse on a single imaging day had peaks at ~1 mM. This resulted in vascular parameters which were, on average, twice as high as parameters from other datasets. Thus, for consistency, we replaced these AIFs with an AIF generated from the same animal on the preceding day. Parameters generated from either AIF did not signifcantly affect subsequent cohort analysis.

The fitted AIF was applied to equation (5.3) to derive K_{trans}, v_e and v_p. Values were fitted for the averaged whole ROI time curve (global ROI) and voxel-by-voxel using a Levenberg-Marquardt nonlinear algorithm implemented in MATLAB. For voxel fitting, voxels that did not converge to a realistic fit (r^2 <0, $K_{trans} \geq 5$, $0 < v_e < 1$ and $0 < v_p < 1$), were removed from further analysis.

The second DCE-MRI dataset on each day was compared to the baseline dataset acquired earlier in the same day.

A sample AIF and tumor curves from a single dataset (with associated model fits) are shown in Figure 5.2.

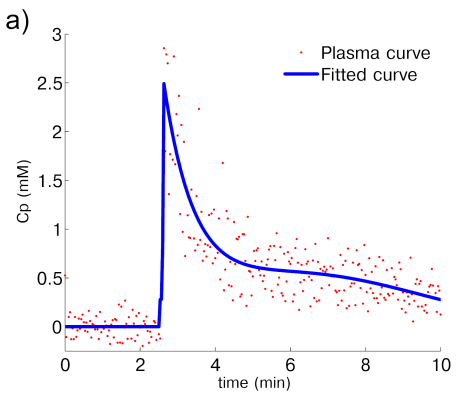

(a) AIF time curve. Raw data in red, model fit in blue.

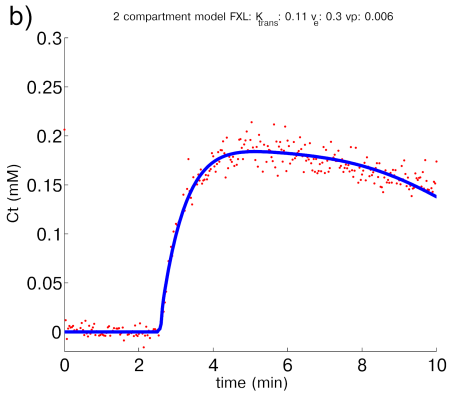

(b) Tumor time curve from ROI drawn over the whole tumor (global ROI). Raw data shown in red, extended Kety model fit shown in blue. Model fit used the AIF shown in a)

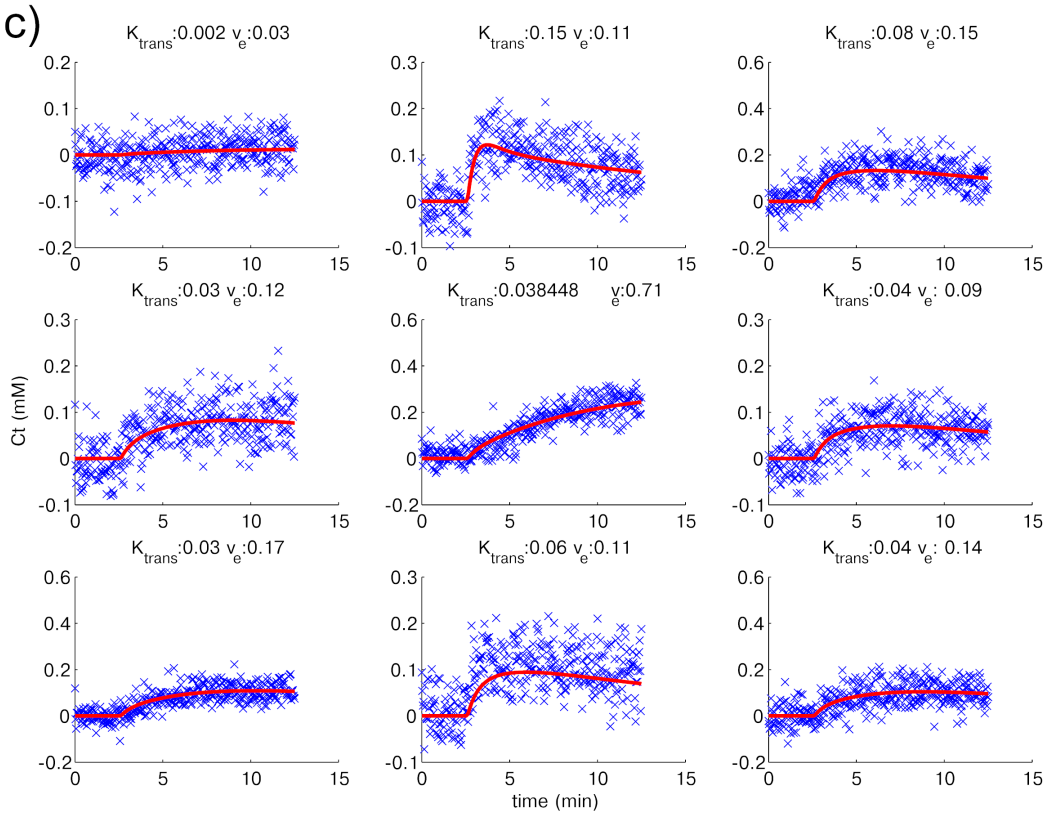

(c) Sample voxel fits from the same tumor as b). Raw data shown in blue, red line denotes Kety model fit. Data was fitted with data from the first 10 minutes, but the fit is shown across 12.5 minutes.

Figure 5.2: AIF, tumor time curves and model fits from Magnevist injection.

A semiquantitative metric, the area under the curve (AUC), was also calculated for each global

ROI and voxel concentration vs. time curve. AUC was calculated using the trapezoidal rule over the course of 8 minutes post CA injection.

5.2.4 PET/MRI studies

A timeline for the PET/MRI studies is shown in figure 5.3. Mice were setup as per the MRI-only studies.

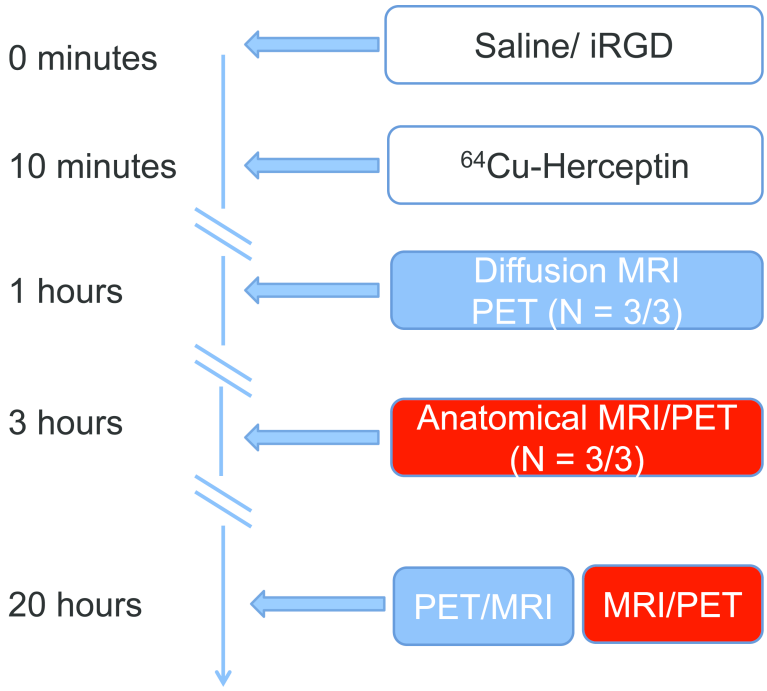

Figure 5.3: Study design for Diffusion MRI/PET. Each BT474-bearing mouse was imaged over the course of 20 hours. Saline or iRGD was injected intravenously 10 minutes before the injection of ^{64}Cu-DOTA-NHS-Herceptin. Simultaneous PET/ diffusion MRI was performed 3 and 20 hours after antibody injection.

5.2.4.1 Anatomical MRI

Anatomical MRI was obtained as per section 5.2.3.1.

5.2.4.2 *In Vivo* PET/MRI

Simultaneous diffusion MRI/ PET was performed with and without iRGD administration. Saline (N = 3) or iRGD (0.5 mg/mouse, N = 3) at a volume of 0.1 mL was injected i.v. , followed by^{64}Cu-DOTA-NHS-Herceptin (3–4 MBq/mouse, i.v.) 10 minutes later. ^{64}Cu-DOTA-NHS-Herceptin was

synthesized as per previous studies [115].

Combined diffusion MRI and PET was obtained 3 and 20 hours post radiolabelled antibody injection. Anatomical MRI was first done to position the tumor in the center of the PET FOV. Diffusion MRI was obtained with a spin-echo sequence (TR/TE=3000/23ms, matrix size = 140 × 80, resolution = 0.25 × 0.25 mm^3, slice thickness = 1 mm, 10 slices, δ/Δ = 3/15ms, b-values = 0, 300, 1000 s/mm^3, 1 direction) and processed as described in section 3.4.3.4. PET was obtained with a duration of 1200s at the 3 hour time point and 1800s at the 20 hour time point.

An additional 6 mice (N = 3 per cohort) were also imaged with anatomical MRI/PET. Images were acquired at 1 and 20 hours after antibody injection. PET was obtained with a duration of 600 and 1800 s at the 1- and 20-hour time points respectively.

5.2.4.3 Image Analysis

PET images were processed and calibrated as described in section 3.4.3. PET and anatomical MRI images were aligned to ADC datasets using the method described in Section 3.2.3.2. Tumor ROIs were drawn on the anatomical MRI images in order to extract tumor ADC and PET uptake values (in units of % ID/g). Due to a hardware malfunction during one of the study days, 20-hour time points PET images were not obtained for 2 saline and 1 iRGD-treated mice. Diffusion MRI were obtained for those animals.

5.2.5 Histological Assessment

iRGD effects on the uptake of Herceptin were assessed by histology. Mice bearing BT474 tumors were injected with saline or iRGD (0.5 mg/ mouse) intravenously. This was immediately followed by an injection of Alexa 633-conjugated Herceptin (0.1 mg, i,v.). Tumor samples were obtained at 1, 3 and 20 hours post Herceptin injection (N = 2 per time point, per treatment). 20 minutes prior to tumor extraction, FITC-labelled Lycopersicon esculentum lectin (0.15 mg per mouse i.v., Vector Laboratories) were injected to visualize perfused vessels. Mice were sacrificed by transcardiac perfusion and tumors were excised. Tumors were placed in 4% paraformaldehyde overnight and then cryoprotected in a sucrose gradient (10%–30%) over three days. Tumors were then embedded in OCT (Sakura) and 20 μm cryosections were obtained.

All tumor slices were stained with DAPI and then visualized using either a 5x/0.15 Ph1 (Plan-Neofluar) objective on a Zeiss LSM 5 Exciter confocal microscope. Five random FOVs were imaged from slides containing slices from each tumor to evaluate antibody uptake.

5.2.6 Statistical Analysis

Two-sided paired t-tests were used to compare iRGD or PAF cohorts to the control cohort. A p-value of 0.05 or smaller was considered to be statistically significant.

5.3 Results

5.3.1 MRI-only Studies

Uptake curves in the tumor were highly heterogeneous (figure 5.4). Thus, we analyzed the tumor both using global ROI-generated parameter values and on a voxel-by-voxel basis. Voxel-by-voxel parametric maps for a mouse treated with saline, iRGD and PAF are shown in figure 5.5.

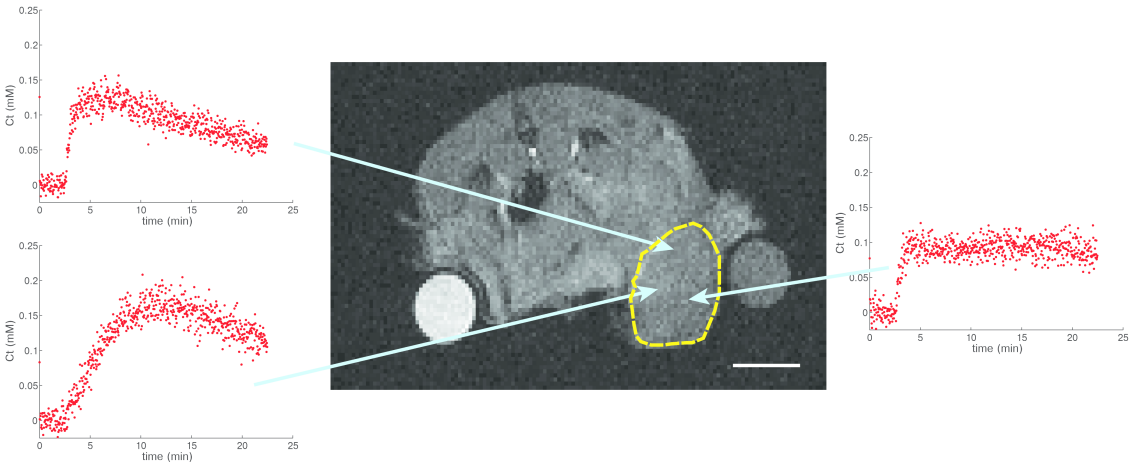

Figure 5.4: Heterogeniety of tumor CA uptake. Curves taken from 3 different ROIs within the tumor shown in figure 5.2 show that different regions of the tumor (outlined in yellow) show different uptake kinetics (scale bar = 5 mm).

Mean K_{trans}, v_e and $v_p$values derived from global and whole (mean from voxels fits obtained for the whole tumor) ROIs are shown in table 5.1. No signifcant differences were observed between baseline values for all treatment cohorts across Days 1–3, suggesting that administration of PAF or iRGD on Day 1 of the study did not have dramatic long term (>12 hours) effects on tumor vascular

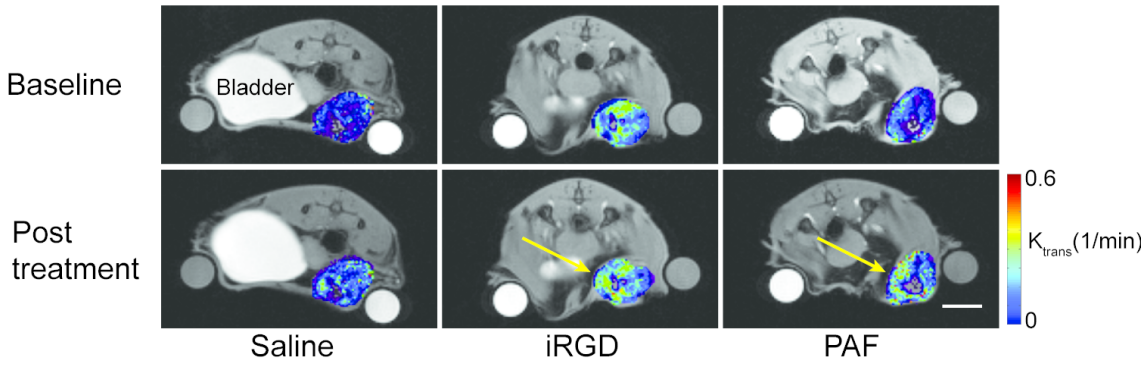

(a) K_{trans} maps for an individual mouse due to different treatments. An increase in K_{trans} was observed after both iRGD and PAF treatment, mostly around the medial side of the tumor (yellow arrows). In contrast, no dramatic increase was seen after saline treatment (scale bar = 5 mm).

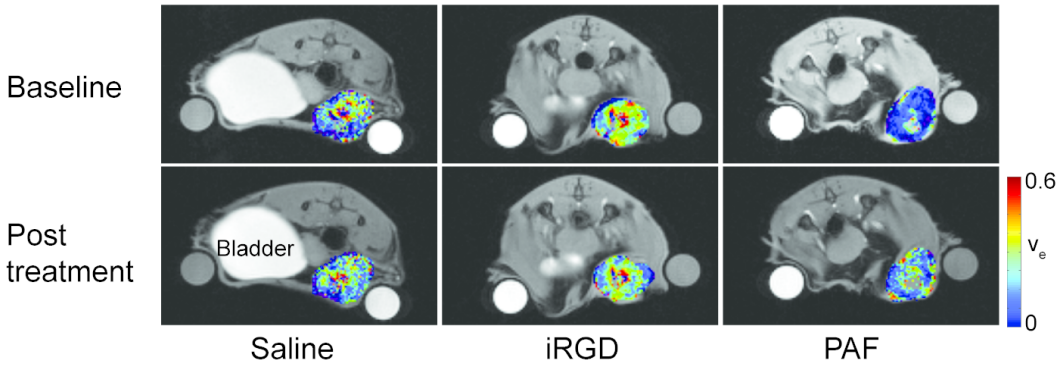

(b) v_e maps for an individual mouse due to different treatments. An increase in v_e was observed after PAF treatment throughout the tumor slice. In contrast, no dramatic increase was seen after saline or iRGD treatment (scale bar = 5 mm).

Figure 5.5: Vascular parametric maps for a single mouse over multiple days.

parameters and justified the study design.

Table 5.1: Mean vascular parameters for different treatment cohorts for global ROI and whole ROI (voxels). Standard errors of the mean are shown. All global fits had a r^2 value greater than 0.98. Although in both ROIs increases in K_{trans} and v_e were observed, these were not statistically significant ($p > 0.05$).

	K_{trans}(1/min)	v_e	v_p	K_{trans}(1/min)	v_e	v_p
saline	0.1±0.02	0.19±0.03	0.01±0.002	0.1±0.02	0.18±0.02	0.01±0.003
iRGD	0.08±0.01	0.16±0.02	0.01±0.002	0.17±0.06	0.24±0.08	0.01±0.002
PAF	0.08±0.01	0.18±0.03	0.01±0.004	0.17±0.06	0.38±0.17	0.02±0.007
	Baseline (AM)			12 minutes posttreatment (PM)		
			Global ROI			
saline	0.13±0.02	0.23±0.02	0.01±0.002	0.12±0.01	0.21±0.01	0.01±0.003
iRGD	0.1±0.01	0.2±0.02	0.01±0.001	0.17±0.04	0.21±0.03	0.01±0.001
PAF	0.11±0.02	0.22±0.03	0.01±0.003	0.2±0.05	0.26±0.03	0.02±0.003
	Baseline (AM)			12 minutes posttreatment (PM)		
			Whole ROI, from voxels			

Table 5.1 shows that both iRGD and PAF caused an increase in both K_{trans} and v_e calculated from a global ROI and also voxels from the whole tumor (whole ROI). However, neither cohort was statistically significantly different from the saline cohort. To account for the intersubject variability of tumor vascular parameters, we calculated the percentage change from baseline of each parameter for each subject and compared these values. These are tabulated in table 5.2. Again, both iRGD and PAF cohorts showed increased percentage changes from baseline values for both K_{trans} and v_e compared to the saline treated cohort. The PAF cohort showed statistically significant increases in K_{trans} (for both global, p <=0.01 and whole ROI, p <=0.01) and v_e (whole ROI, p = 0.02) compared to the control cohort.

Table 5.2: Mean percentage change from baseline of vascular parameters for both global ROI and whole ROI (voxels). SEMs are shown. * and ** denote significant differences with the saline cohort ($p <= 0.01$ and $p = 0.02$ respectively).

% change from baseline	K_{trans}	v_e	v_p	K_{trans}	v_e	v_p
saline	14±20	3.7±8.9	78±40	10±16	-1.9±7.4	36±21
iRGD	94±63	32±33	45±20	56±28	4.5±9.4	6.7±9.4
PAF	105±32 *	77±38	137±78	80±25 *	23±10 **	73±32
		Global ROI			Whole ROI, from voxels	

Heterogeniety of treatment response was probed further by segmenting the tumor. Two segmentation criteria were examined. First, voxels from each tumor were sorted into percentile bins

according to K_{trans} values (e.g.top 10% K_{trans} values, top 10%–20% K_{trans} values etc.). Percentage changes from baseline of both K_{trans} and v_e for each percentile bin were compared between treatment cohorts. These comparisons are shown in figure 5.6. K_{trans} values after PAF treatment generally increased across all K_{trans} percentile bins. In contrast, K_{trans} increases after iRGD treatment were greater for highly enhancing voxels (higher K_{trans} bins) compared to the lower enhancing voxels (low K_{trans} bins). V_e increases due to PAF were greater for highly enhancing voxels compared to lower enhancing voxels, while v_e did not change from the baseline for the iRGD cohort.

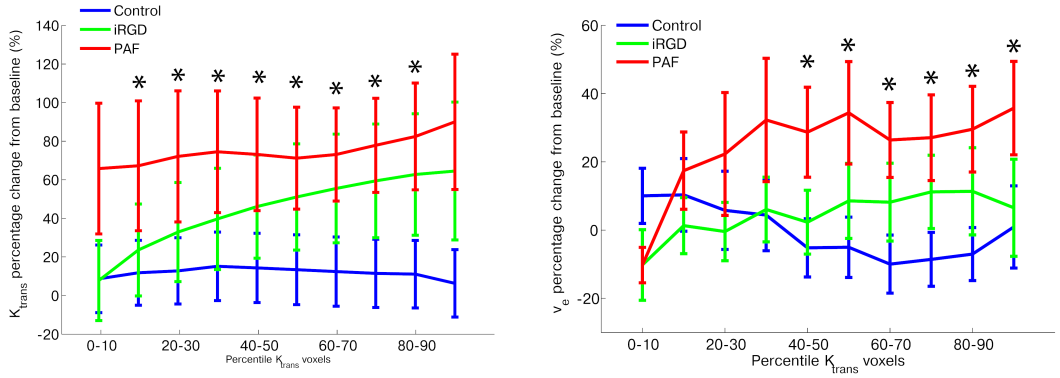

(a) K_{trans} percentage change.

(b) v_e percentage change.

Figure 5.6: Mean percentage change from baseline, sorted by tumor K_{trans} value. Stars (*) denote that PAF treatment was significantly different to the saline control (p <0.04). Error bars denote SEM.

Next, voxels from each tumor were sorted based on their distance from the tumor edge, which was determined based on the ROI mask. Percentage changes from baseline of both K_{trans} and v_e as a function of distance from the tumor edge were compared between treatment cohorts. These comparisons are shown in Figure 5.7. K_{trans} increases from the baseline were consistent regardless of the distance from the edge of the tumor for both PAF and iRGD cohorts. This was also the case for v_e increases observed in the PAF treated cohort.

AUC parameters calculated for the global ROI and the whole ROI are shown in table 5.3 and table 5.4. While not statistically significant, AUC results showed similar trends to compartmental modeling results, showing an increase in CA uptake post iRGD and PAF treatment compared to the saline controls.

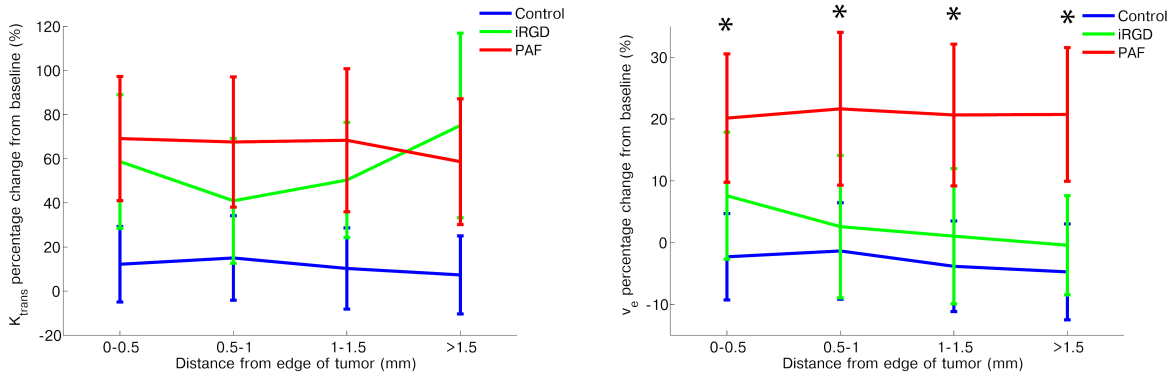

(a) K_{trans} percentage change.

(b) v_e percentage change.

Figure 5.7: Mean percentage change from baseline, sorted by distance from the tumor edge. Stars (*) denote that PAF treatment was significantly different to the saline control (p <0.04). Error bars denote SEM.

Table 5.3: Mean AUC calculated over 8 minutes post CA injection for different treatment cohorts for global ROI and whole ROI (voxels). Standard errors of the mean are shown. Although both iRGD and PAF cohorts showed increases in AUC, these were not statistically significant (p >0.05). AUC had units of mM min.

	AUC_{pre}	AUC_{post}	AUC_{pre}	AUC_{pre}
saline	0.16±0.02	0.16±0.02	0.17±0.02	0.16±0.02
iRGD	0.14±0.02	0.21±0.07	0.14±0.02	0.22±0.07
PAF	0.15±0.03	0.32±0.13	0.16±0.03	0.33±0.13
	Global ROI		Whole ROI, from voxels	

Table 5.4: Mean percentage change from baseline of AUCs for both global ROI and whole ROI (voxels). SEMs are shown. AUC had units of mM min.

% change from baseline	$AUC_{Global\,ROI}$	$AUC_{whole\,ROI}$
saline	6±10	5±10
iRGD	40±37	42±37
PAF	78±32	77±31

5.3.2 PET/MRI Studies

PET/MRI images acquired at different time points for saline-treated and iRGD mice are shown in figures 5.8 and 5.9. A general trend from low to high antibody uptake over time was observed regardless of treatment. For the particular mice shown, higher antibody uptake in the tumor was observed at all time points when treated with iRGD. Interestingly, the spatially matched diffusion MRI images showed that high ADC values were present in the iRGD-treated tumor. Lower ADC values were present in the time matched saline-treated control.

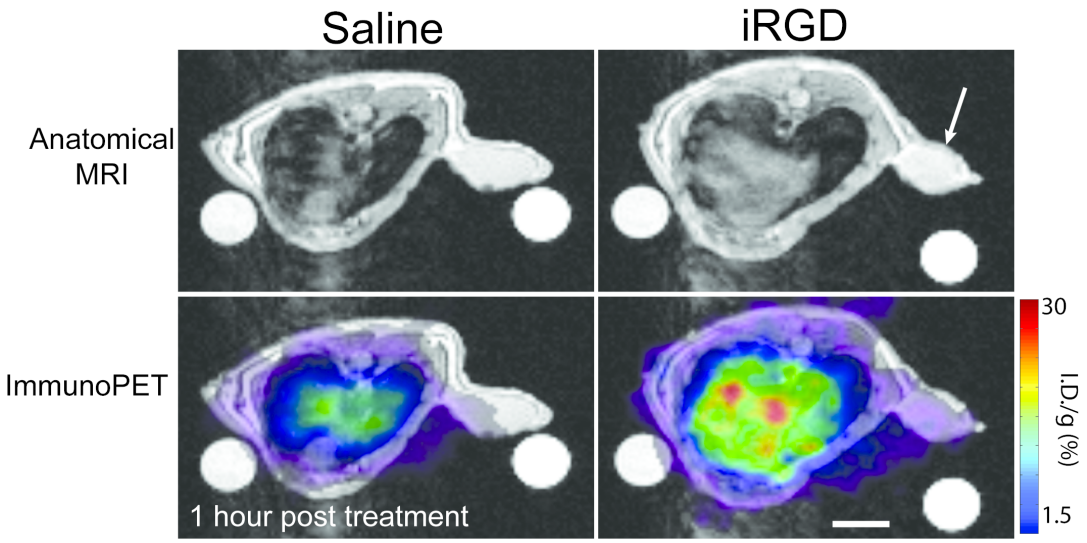

Figure 5.8: PET/MRI of radiolabelled-Herceptin uptake 1 hour post saline/iRGD treatment and antibody injection. At 1 hour, most of the antibody was still in the systemic circulation, as demonstrated by the high activity in the torso. A small but significant increase in antibody uptake within the iRGD-treated (most of the tumor contained activity at the image threshold level) tumor compared to saline-treated control (half the tumor does not show any activity at the image threshold level) was observed. Arrow points at the tumor (scale bar = 5 mm).

Mean ADC and antibody uptake values across both treatment cohorts are shown in tables 5.5 and 5.6. Maximum antibody uptake values are shown in table 5.7. No significant difference in mean ADC values were observed between treatment cohorts at all time points. A 50% increase in mean antibody uptake in iRGD-treated animals compared to the control animals 1 hour after treatment and antibody injection (p <0.02) was observed. However, by 3 and 20 hours, no difference was seen between the two cohorts. No significant difference in the maximum tumor PET uptake value was observed between the two cohorts at all time points.

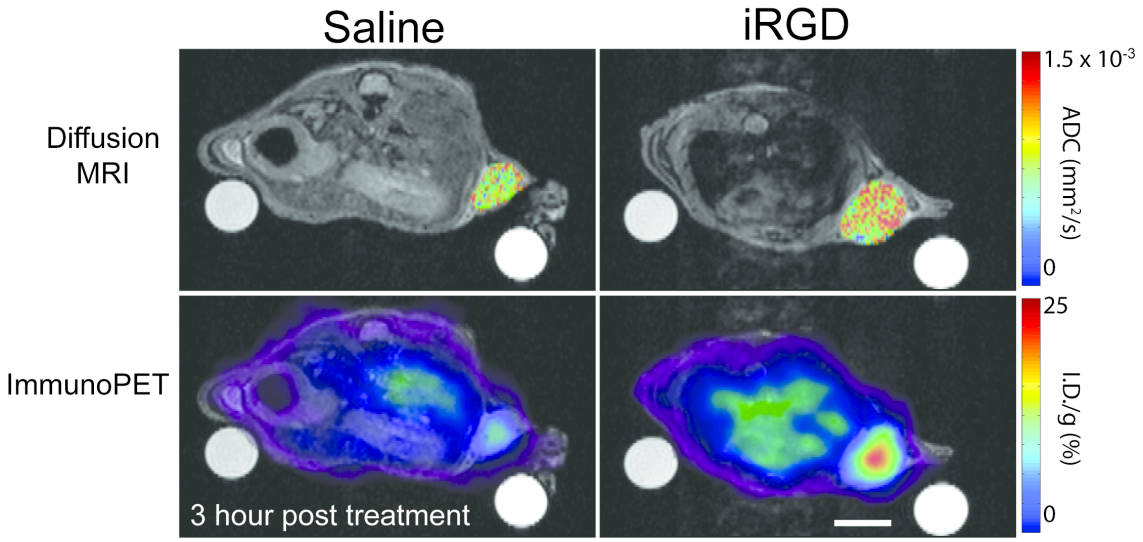

(a) 3 hours posttreatment/ antibody injection in a saline control and iRGD-treated mouse. This particular iRGD-treated mouse showed high antibody uptake in the tumor compared to the saline control. Correspondingly, the tumor ADC values were also higher in this mouse compared to the saline control (scale bar = 5 mm).

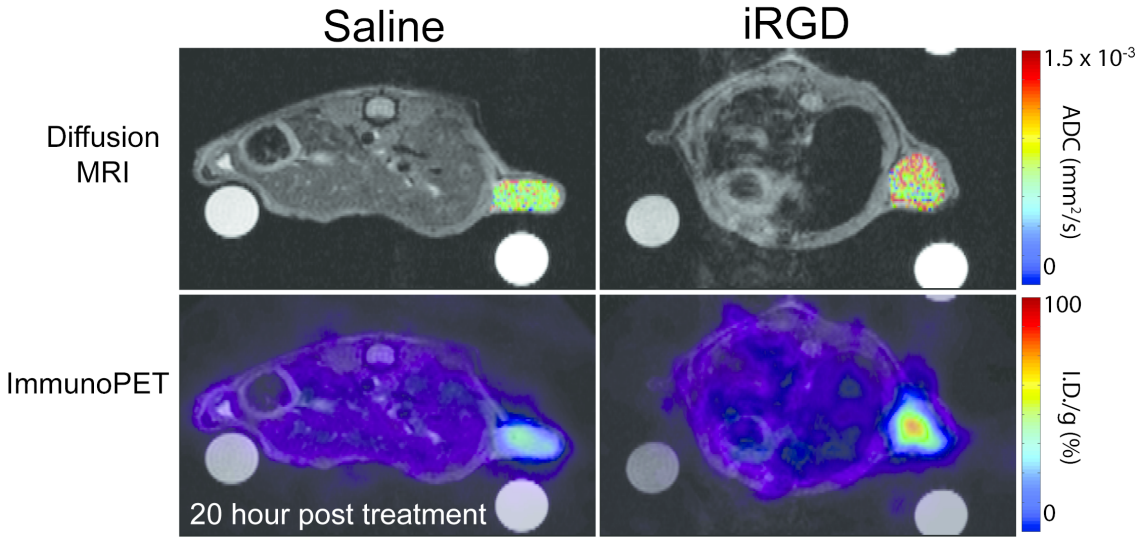

(b) 20 hours posttreatment/ antibody injection in a saline control and iRGD-treated mouse. This particular iRGD-treated mouse showed high antibody uptake in the tumor compared to the saline control. Correspondingly, the tumor ADC values were remained higher in this mouse compared to the saline control.

Figure 5.9: PET/ Diffusion MRI of radiolabelled-Herceptin uptake 3 and 20 hours post saline/iRGD treatment and antibody injection. This particular iRGD-treated mouse showed high antibody uptake. However, no significant differences of ADC or PET uptake were observed between the iRGD and saline cohorts.

Table 5.5: Mean tumor ADC values at 3 and 20 hours post iRGD treatment. No significant differences between cohorts were observed. Errors denote SEM.

$x10^{-3}mm^2/s$	3 hours	20 hours
saline	1.27±0.1	1.18±0.1
iRGD	1.22±0.2	1.23±0.2

Table 5.6: Mean tumor PET uptake values at 3 and 20 hours post iRGD treatment. Mean antibody uptake in iRGD treated animals was significantly higher than controls at the 1 hour time point (*, p <0.02). Errors denote SEM.

% ID/g	1 hour	3 hours	20 hours
saline	1.62±0.1	6.76±0.1	20.9±2.5
iRGD	2.55±0.2*	7±1.8	18.8±5.7

Table 5.7: Maximum tumor PET uptake values at 3 and 20 hours post iRGD treatment. Errors denote SEM.

% ID/g	1 hour	3 hours	20 hours
saline	4.25±0.3	8.50±1.5	53.5±8.8
iRGD	6.90±1.1	15.1±7.7	56.6±20.5

5.3.3 Histological Assessment

Sample immunofluoresence images of optically labelled Herceptin antibody are shown in figures 5.10 and 5.11. Qualitatively, iRGD-treated tumors showed higher antibody uptake compared to the saline cohorts across all time points. However, high antibody uptake was also observed in certain saline-treated tumors. intratumoral antibody distribution patterns can be also be variable (figure 5.12).

5.4 Discussion

The ability to identify iRGD-responsive patients prior to treatment will facilitate iRGD's path to translation and maximize its patient impact. Several approaches can be used for this process. A tumor biopsy can identify the presence of the putative targets of iRGD, α_v integrin and neuropilin-1 receptors. However, information about the heterogeneous spatial expression of these markers, an important determinant for efficacy [265, 266], may not be available with this technique. Moreover, biopsies cannot be obtained with sufficient time resolution to gauge the efficacy of the iRGD response (~hours).

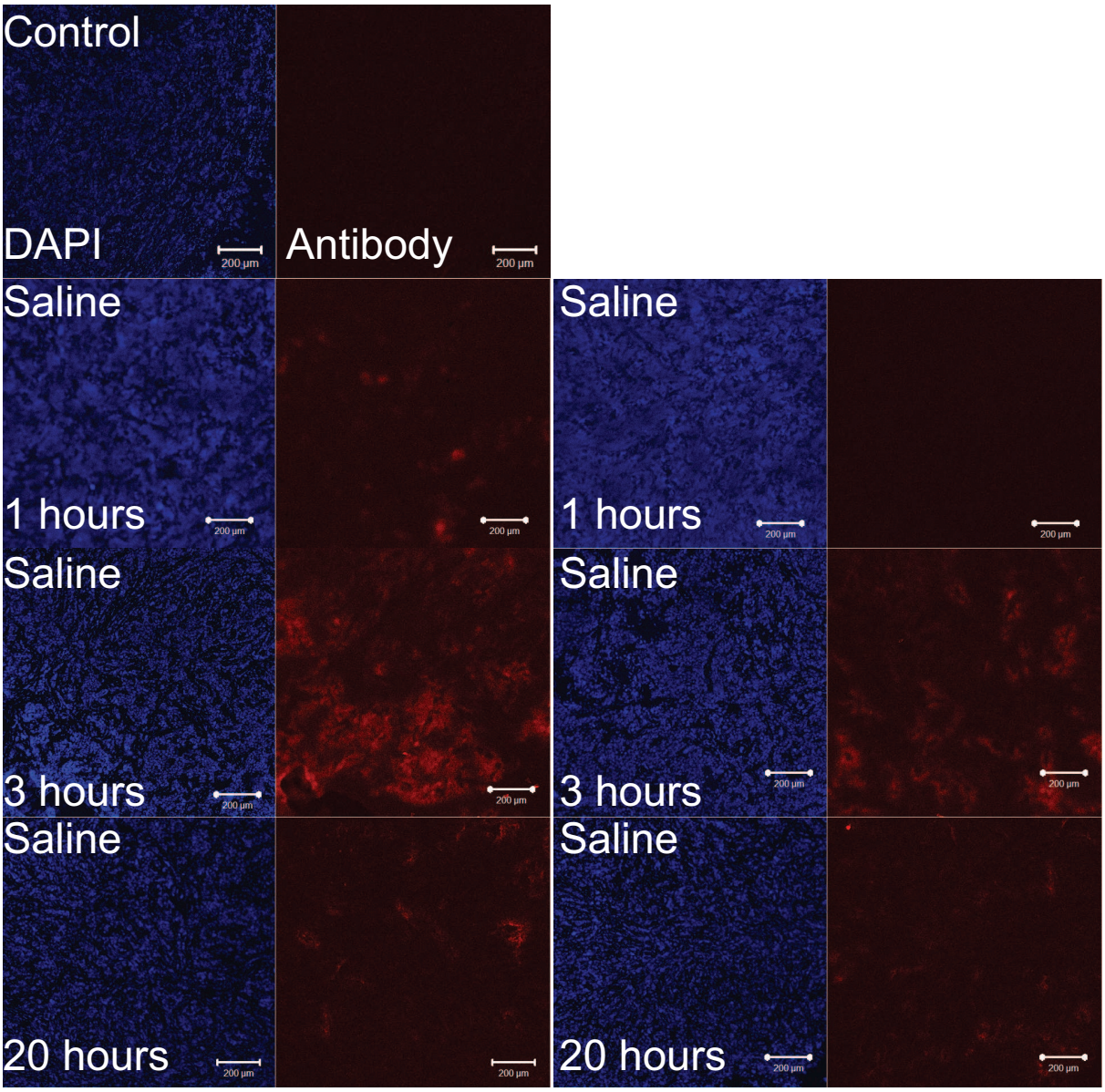

Figure 5.10: Immunofluoresence of antibody uptake with saline. Alexa-633 Herceptin antibody injected into saline-treated BT474 mice over the course of 20 hours. Tumors were harvested at various time points post injection. Images were all acquired using the same laser and aperture settings. Images with the highest antibody signal from each slide are shown on the left. Regions with lower uptake from the same slide are shown on the right. Some saline-treated tumors did show high antibody uptake (seen here especially at the 3 hour time point). A control tumor with no antibody injected is presented. Lycopersicon esculentum lectin signal was variable across all tumors and thus is not presented (scale bars = 0.2 mm).

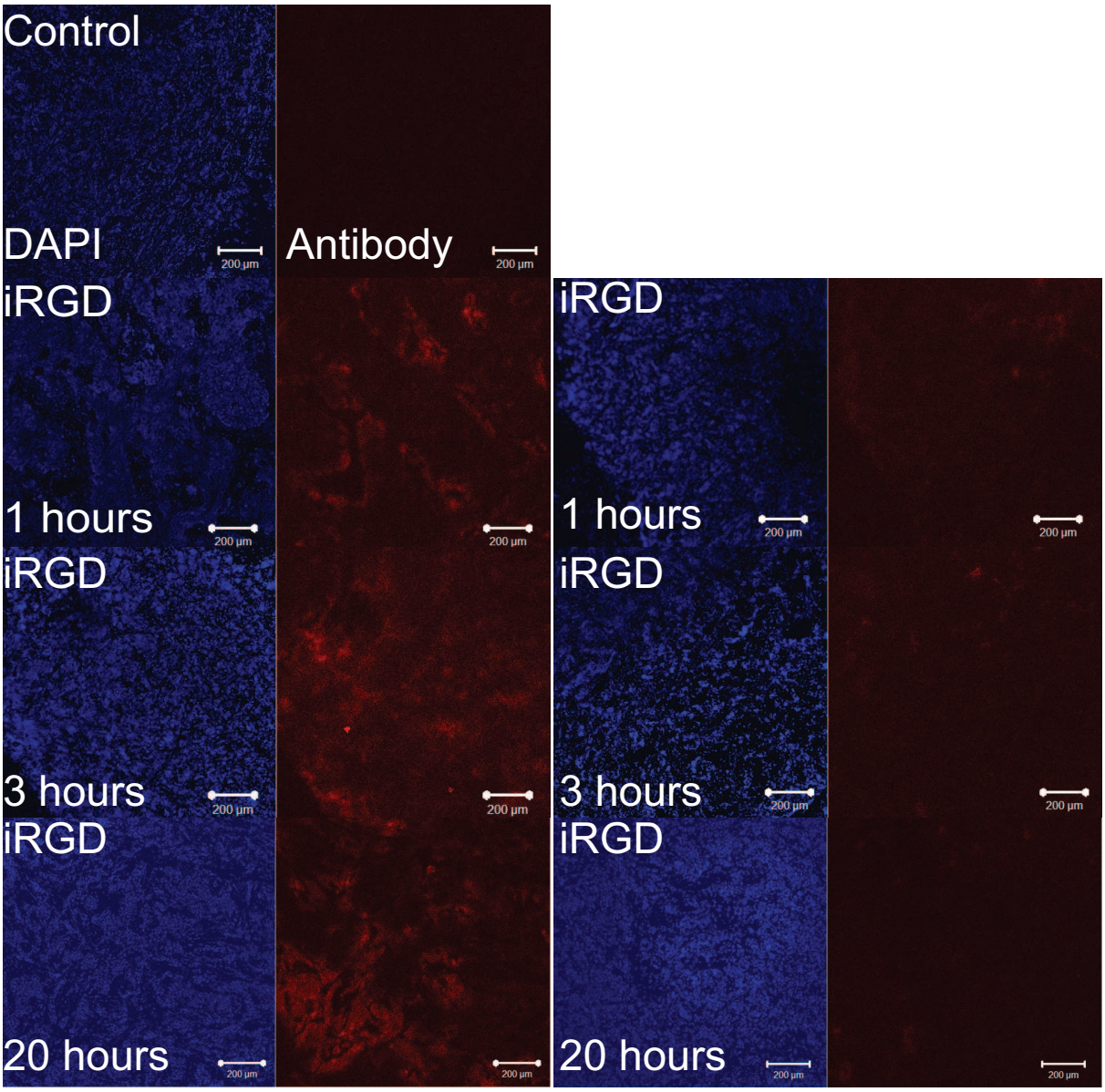

Figure 5.11: Immunofluoresence of antibody uptake with iRGD. Alexa-633 labeled Herceptin antibody was injected into BT474 mice with iRGD over the course of 20 hours. Tumors were harvested at various time points post injection. Images were all acquired using the same laser and aperture settings. Images with the highest antibody signal from each slide are shown on the left. In general, an increased uptake of antibody was observed over the course of 20 hours, with more uptake visible in iRGD-treated animals compared to saline controls. A control tumor with no antibody injected is presented. Lycopersicon esculentum lectin signal was variable across all tumors and thus is not presented (scale bars = 0.2 mm).

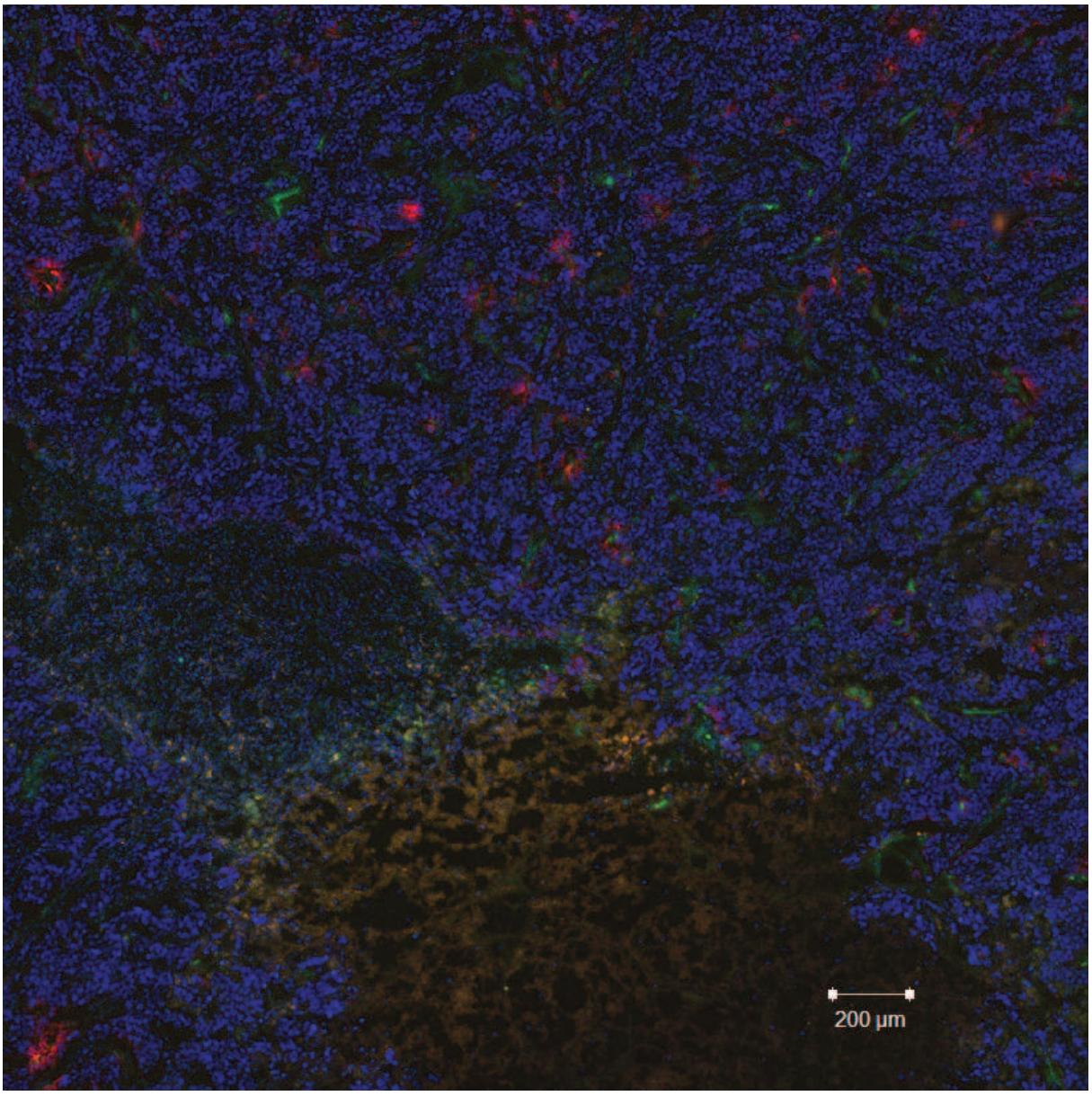

Figure 5.12: Tiled images of a BT474 tumor treated with iRGD and Alexa-633 labelled Herceptin antibody and harvested 3 hours post injection. Distribution of antibodies (red) vary greatly across the tumor, with several concentrated regions of antibody uptake (blue: DAPI, green: lycopersicon esculentum lectin, orange: matrigel plug, scale bar = 0.2 mm).

Noninvasive imaging represents an interesting alternative approach to monitor iRGD efficacy. In particular, MRI can provide high-resolution images of tumor tissue with no ionizing radation. Further, dynamic MRI can monitor physiological changes in the tumor in real time.

5.4.1 DCE-MRI

We designed the DCE-MRI protocol used in this study with consideration for its direct clinical applicability. Gd-DTPA is a clinically approved CA which is widely used to quantitatively evaluate tumor vascular permeability preclinically and clinically and has a short plasma half-life (<12 minutes in murine models). Since iRGD was shown to improve the uptake of small molecule doxorubicin [49], we hypothesized that it would also increase the uptake of Gd-DTPA. Pre- and posttreatment DCE-MRI scans were obtained in the same animal to account for the tumor response variability between subjects; a critical factor for patient studies. This variablity also motivated the need to treat the same tumor with all three different conditions. A key assumption made here is that PAF and iRGD have short acting time windows (<12 hours). We believe that this was reasonable based on previous reports showing that both PAF and iRGD have high activity within 3 hours of administration [267, 49]. Other classes of small molecule vasoactive agents also have short time windows of action (<3 hours) [258]. Furthermore, the plasma half-life of iRGD in mice is less than 10 minutes (private communication, A.R.), suggesting that very little, if any, peptide will be in circulation more than 12 hours post administration. The fact that baseline DCE-MRI parameters for different treatments, which were obtained on separate days, did not differ significantly from each other also supported this assumption. Baseline scans were also obtained to account for intrasubject variabilty of DCE-MRI parameters over time, since this may change relatively quickly (~days) during the natural progression of preclinical tumor models [268].

Preliminary DCE-MRI results presented here suggest that DCE-MRI can monitor systemic adminstration of a potent vascular permeability modulating agent. Significant increases in vascular permeability (K_{trans}) and tumor extracellular volume (v_e) compared to saline control were observed in PAF-treated mice (table 5.2). PAF was chosen as the positive control in this study based on previous reports describing the ability of localized [269, 270] and systemically adminstered PAF [271, 267] to increase vascular permeability in a variety of tissues [272, 273]. Moreover, VEGF

pathway activation has been implicated as a factor for this increase [272, 273]. The neuropilin-1 receptor, which interacts with the cleaved-iRGD product, is also involved in the VEGF pathway [274, 243, 275, 244], specifically by increasing tissue vascular permeability [276, 277, 246]. We chose to deliver PAF systemically to mimic the administration of iRGD; the dose was chosen based on previous reports [271, 267] and preliminary toxicity studies. Increases in both K_{trans} and v_e are consistent with PAF's ability to increase tissue vessel permeability and to cause localized inflammation which would lead to delayed CA washout.

On average, iRGD-treated tumors showed a slight increase in K_{trans} above baseline compared to saline treatment, but this increase was not significantly different. This suggested that a vascular permeability effect is present, but is lower than that effected by PAF. No observable v_e deviations from baseline was seen. The latter observation suggests that the extracellular space in the tumor does not expand due to iRGD, suggesting that the CA may be taken up by cells.

Since vascular permeability parameters (and changes compared to baseline) were heterogeneous throughout the tumor (figure 5.5), we stratified tumor voxels according to the presence of viable vessels (defined by K_{trans}) and distance from the tumor edge. PAF caused a signficant increase in all K_{trans} values across the whole tumor, highlighting its potency. In contrast, K_{trans} increases were greater in iRGD-treated tumors as a function of voxel K_{trans} status. Tumor voxels with higher K_{trans} values most likely contain higher density of viable vessels. Thus, increases in vascular permeability should be most visible in these regions. *Ve* did not change at the lowest K_{trans} voxels, corresponding to poorly enhancing regions. V_e increases observed for PAF-treated tumors are consistent across other K_{trans} values. We did not observe any trends in K_{trans} or v_e values as a function of distance from the tumor edge. Voxels were analyzed only if a reasonable parameters were able to be fitted. Thus, the matrigel plug and obvious central necrotic regions that are visible in certain tumors were excluded from analysis.

A semiquantitative metric, AUC, showed similar trends between cohorts as the pharmacokinetic model parameters. Along with the good model curve fits (figure 5.2), this suggests that pharmacokinetic modeling can be applied to the current dataset.

Quantitative DCE-MRI, especially in small animals, is challenging. Several factors can affect the output parameter values. To keep relatively good spatial coregistration between pre and

posttreatment DCE-MRI data, mice were kept lightly anesthetized in the animal holder between imaging sessions. Isofluorane is a vasodilator and increases vascular permeability via caveolae transport [278]. Studies with Gd-DTPA-Albumin showed that anesthesia induction with isofluorane can cause increased CA extravasation from vessels [279]. A study with a similar protocol as our study (maintainance of anesthesia using 2% isofluorane for 4–5 hours) did not show a demonstratable K_{trans} increases between the two imaging sessions [280]. Caveolae are not necesary for the hyperpermeable tumor vascular phenotype [281], but their role in iRGD activity remains unknown. Another confound is the acquisition of the AIF. Image-derived AIF can be corrupted by flow and motion artifacts. AIFs used in this study were comparable to literature [264, 263]. A population-based AIF or the use of a reference region based DCE-MRI analysis method [84] can be used to verify the consistency of these results. The small size and contrast generating mechanism of Gd-DTPA may also have confounded results. Since tumor vasculature is hyperpermeable, Gd-DTPA may leak through the tumor vessels regardless of the presence of iRGD. Although not clinically approved, larger-sized CA such as Gd-DTPA-Albumin may be more sensitive to permeability changes [282]. Further, the long half-life of such agents may enable the pharmacodynamics of iRGD to be visualized. Previous results suggest that iRGD may mediate uptake of agents by tumor cells [48]. The lack of obeservable v_e increase supports this. Signal intensity changes caused by intracelluar Gd-agents are significantly attenuated compared to their extracellular counterparts, since the water compartment within organelles and the cytoplasm are small and water exchange with external compartments can be slow [283]. An alternative method of MRI visualization that is less affected by these issues is the use of R_2^* -agents such as iron oxide particles [284, 78]. Studies using these different types of agents are being pursued in the lab.

5.4.2 PET/MRI

Sugahara *et al.* showed that iRGD increased Herceptin uptake in BT474 tumors [49]. Thus, we hypothesized that this uptake could be observed with PET, coregistered with diffusion MRI. The DCE-MRI protocol in the MRI-only study was not used here because its MRI gradient requirements made temperature control of the PET difficult. Diffusion MRI can be sensitive to sudden changes in vascular permeability [285]. We hypothesized that this technique may also be sensitive to iRGD

effects.

While certain animals treated with iRGD did show increases in both ADC values and radiolabelled antibody uptake (figures 5.8 and 5.9), no significant differences were observed for either biomarker between saline and iRGD-treated cohorts overall. An increase in antibody uptake for iRGD-treated animals compared to control was present 1 hour post injection, but the difference was not prolonged into later time points. Unfortunately, no ADC images were acquired with the 1 hour PET images; so no intratumoral structural information was available to guide our PET image interpretation.

Histological results were variable. Visual inspection of random tumor regions suggested that slightly higher antibody uptake was present overall in iRGD-treated tumors. Yet there were some saline-treated tumors that also exhibited high antibody uptake. Antibody distribution showed high intratumoral variability. A method that allows histological visualization of large tumor volumes, such as the VIBRA-SSIM technology (D. Koos, S. Fraser, Caltech), would complement current imaging studies by providing a complete picture of tumor microstructure and intratumoral antibody uptake.

5.4.3 Conclusions

Preliminary results outlined in this chapter did not show dramatic changes in vascular permeability (using DCE-MRI) nor antibody uptake (using PET and optical imaging) due to iRGD. Concurrent studies using the same mouse tumor model, using luciferase, different radiolabelled agents (e.g.minibodies) and treatment response as alternative readouts of iRGD reported similar variable results (private communication, A.R.). Several issues need to be considered when evaluating these results apart from those discussed above. Firstly, PET and MRI may be too insensitive to the changes caused by iRGD. If the changes occur in concentrated regions within the tumor, then partial volume effects may average out the iRGD effects. The heterogeniety of tumor iRGD response, as observed in the DCE-MRI results presented here, is an important factor that needs to be considered and may explain the variability of the histology and the results from the communicated treatment response studies. Secondly, the current iRGD is monovalent. This may not efficiently activate the neuropilin-1 receptor, since its signalling requires dimerization or multimerization [50]. A mul-

timeric form of iRGD may interact with neuropilin-1 better than monomeric iRGD and result in enhanced downstream effects. Another consideration is the applicability of the mouse tumor model for these studies. Tumor growth in mice are much faster than in humans. Thus, one would expect the angiogenic process to be quite different to human tumors too. BT474 was chosen as the model system based on previous reports showing the good neuropilin-1 receptor expression in this cell line [48] and good iRGD response [49]. However, other investigators reported that BT474 actually show low neuropilin-1 expression in their hands [286]. Others have also reported that $\alpha_v\beta_3$ integrin expression are low in BT474 tumors [287]. This suggests that the development of suitable cancer mouse models for certain applications remains very challenging. Human tumor pathology and treatment response may be significantly different to their animal counterparts. Of course, our discussion assumes that the proposed mechanism of action of iRGD is accurate. In light of these results, it will be important to elucidate and verify iRGD's mode of action in more basic studies.

Ultimately, the clinical efficacy of iRGD and the applicability of noninvasive imaging to monitor iRGD effects may only be determined by pursuing human studies. Imaging and analysis techniques developed in this chapter will be directly applicable to these pursuits.